Dual-Templating Approaches to Soybeans Milk-Derived Hierarchically Porous Heteroatom-Doped Carbon Materials for Lithium-Ion Batteries

Peng Yan,[a] Huaibo Ye,[a] Yang Han,[a] Jingjing Wang,[a] Fenfen Zheng,[a] Weiwei Xiong,*[a] Hongxun Yang,[a] Junhao Zhang,[a] Aihua Yuan,*[a] and Xingcai Wu*[b]

Biomass derived carbon materials are widely available, cheap and abundant resources. The application of these materials as electrodes for rechargeable batteries shows great promise. To further explore their applications in energy storage fields, the structural design of these materials has been investigated. Hierarchical porous heteroatom-doped carbon materials (HPHCs) with open three-dimensional (3D) nanostructure have been considered as highly efficient energy storage materials. In this work, biomass soybean milk is chosen as the precursor to construct N, O co-doped interconnected 3D porous carbon framework via two approaches by using soluble salts (NaCl/ Na$_2$CO$_3$ and ZnCl$_2$/Mg$_5$(OH)$_2$(CO$_3$)$_4$, respectively) as hard templates. The electrochemical results reveal that these structures

were able to provide a stable cycling performance (710 mAh·g^{-1} at 0.1 A·g^{-1} after 300 cycles for HPHC-a, and 610 mAh·g^{-1} at 0.1 A·g^{-1} after 200 cycles for HPHC-b) in Li-ion battery and Na-ion storage (210 mAh·g^{-1} at 0.1 A·g^{-1} after 900 cycles for HPHC-a) as anodes materials, respectively. Further comparative studies showed that these improvements in HPHC-a performance were mainly due to the honeycomb-like structure containing graphene-like nanosheets and high nitrogen content in the porous structures. This work provides new approaches for the preparation of hierarchically structured heteroatom-doped carbon materials by pyrolysis of other biomass precursors and promotes the applications of carbon materials in energy storage fields.

1. Introduction

The development of a highly efficient, low cost energy storage technology is critical for the the large-scale application of intermittent renewable energy sources such as wind and solar power. Lithium/Sodium ion batteries (LIBs, SIBs) have been considered as one of the most advanced secondary batteries. Owing to their high energy and long cycle life, they have been widely applied in electric vehicles, portable devices, and grid storage. Today's commercial LIBs use graphite as the anode material. However, the graphite always encounters disadvantages such as low theoretical specific capacity (372 mAh·g^{-1}) and limited rate performance and poor long-term stability. To

solve these problems, it is necessary to develop carbon materials with better performance. As far as we know, carbon matrix such as graphene,[2–4] carbon nanotube,[5] carbon nanofiber,[6] carbon aerogel[7,8] and activated carbon[9–13] materials have been extensively studied. These materials typically exhibit superior electrochemical performance in lithium-ion batteries,[14–17] sodium-ion batteries,[14,18,19] and supercapacitors.[20–24] Hierarchical porous carbon material is an attractive carbon anode material. Their rich pore structure and large specific surface area can provide efficient lithium ion diffusion channels and a large number of active sites. The specific structures also help to reduce the stress during lithium insertion and extraction, improve the rate performance of materials. Therefore, it is highly desired to develop novel hierarchically porous heteroatom-doped carbon materials with remarkable electrochemical properties.

In recent years, biomass derived porous carbon materials have shown great advantage in the application of energy storage due to their unique pore structure, diverse surface functional groups, natural richness and environmental friendliness.[20,21,25–29] More importantly, most biomass is rich in heteroatoms (e.g. N, O, P and S) that can in situ dope into the carbon lattice during the pyrolysis carbonization process. The introduction of heteroatoms helps to improve the electrical conductivity and surface wettability of the material, thereby improving its rate performance for the electrode material. Various synthetic methods have been developed to control the structural features of the biomass-derived electrode materials, including templating method,[28,30] hydrothermal carbonization,[27] and activation method[21] among others. These

[a] P. Yan, H. Ye, Y. Han, J. Wang, F. Zheng, W. Xiong, H. Yang, J. Zhang, A. Yuan
School of Environmental & Chemical Engineering
Jiangsu University of Science and Technology Zhenjiang
Jiangsu 212003 (P. R. China)
E-mail: xiongweiwei@just.edu.cn
         aihua.yuan@just.edu.cn
[b] X. Wu
School of Chemistry and Chemical Engineering
Nanjing
University
Nanjing 210023 (P. R. China)
E-mail: wuxingca@nju.edu.cn

ChemistryOpen

Full Papers
doi.org/10.1002/open.202000081

Chemistry Europe
European Chemical
Societies Publishing

methods can effectively adjust the pore structure, surface properties and degree of graphitization of the biologically derived porous carbon material. Soybean is a crop with high nitrogen content, which is widely cultivated in the world. Recently, researchers have done some research on soybeans and soybean husks and turned them into electrode materials.[31,32] However, the biomass-derived carbons generally have few macropores and mesopores, which limit ion diffusion and electrolyte impregnation of the electrode materials.

The templating method is effective for preparing high-quality porous carbon materials with controllable morphology and desirable pores in appropriate size and shape. Carbonizing the mixture of biomass precursors and suitable templates is a practical strategy for large-scale production of hierarchically structured heteroatom-doped carbon materials. We can easily obtain hierarchical micro-/meso-/macroprous carbon materials through the dual-templating approaches. However, the single salt methods often cannot achieve such results. Here we show two general dual-templating strategies to fabricate hierarchically porous heteroatom-doped carbon materials by using soybean milk as carbon and heteroatoms sources. The mixture of soluble salts ($NaCl/Na_2CO_3$ and $ZnCl_2/Mg_5(OH)_2(CO_3)_4$) is employed as hard templates for the synthesis of hierarchical porous heteroatom-doped carbon materials (HPHCs), possess 3D ordered network structure. Moreover, the HPHCs exhibited superior energy storage capacity and great rate stability when utilized as the electrode of lithium battery.

2. Results and discussion

The schematic diagram of the preparation process of the HPHCs anode is shown in Figure 1. Herein, soybean milk is explored as a novel biomass precursor because of its high nitrogen protein content.[33] The soaked soybeans are firstly made into soybean milk, then thoroughly mixed with the salt and the three-dimensional (3D) structure is formed through a freeze-drying process. After carbonization, the carbon precursor homogeneously coated on the surface of the salts template recrystallization-self-assembly during freeze-drying is converted into a 3D heteroatom porous carbon network. During which the soluble salt not only promotes the graphitization degree of the as-prepared carbon,[34–36] but also functions as a template to produce hierarchically porous structure.[37,38] The hierarchical porous structures can enable large specific surface areas, and

act as ion buffering reservoirs to minimize the diffusion distance of electrolyte ions to the interior surface.[38–40] In addition, it is important to note that N and O atoms in the precursor will in situ dope into the HPHCs, especially the N atoms. Heteroatom doping has been reported can benefit the surface wettability, improve electrical conductivity, generate more active sites, and expand the interlayer distance of the carbon materials.[41–43] Therefore, the templating method is effective to obtain a hierarchical porous carbon material with a large specific surface area and rich N-heteroatoms, which is expected to have better capacitive performance for LIB application.

The morphology of the HPHCs was examined by scanning electron microscopy (SEM) and transmission electron microscopy (TEM), as shown in Figure 2. With the assistance of the salt template, HPHCs are interconnected to form a three-dimensional hierarchical structure, exhibiting a honeycomb-like and analveolate-like morphology with abundant and uniform pores for HPHC-a and HPHC-b, respectively, which is beneficial to electrolyte infiltration and diffusion of ions. Figure 2B and 2G shows that the HPHC-a has distinct corners and edges with a thin carbon wall. The crystal structure of the salt template ($NaCl/Na_2CO_3$) can be preserved after carbonization, indicating that this method is suitable for preparing hierarchical porous carbon materials (Figure S1). The morphology of the carbonized samples is similar at different temperatures, with honeycomb structure, which is completely different with the block carbon obtained without adding salt template (Figure S1). Unlike HPHC-a, HPHC-b presents an alveolate-like morphology with abundant nanopores (Figure 2D, E). The samples were further characterized by high-resolution transmission electron microscopy (HR-TEM). HPHCs showed some ordered layered structures, indicating that the sample had a partially graphitized carbon structure (Figure 2C, F). Figure 2 (I, J, K) shows that C, N, O are uniformly distributed in HPHC-a, demonstrating that the heteroatoms are successfully remained in the carbon matrix after carbonization. Energy-dispersive X-ray spectroscopy (EDS) test further confirmed that there is no impurity phases or residues in HPHC-a (Figure S2) [44].

The structure of HPHCs was further investigated and analyzed by XRD, Nitrogen adsorption/desorption isotherms and Raman spectra. As shown in Figure 3a, the XRD patterns of
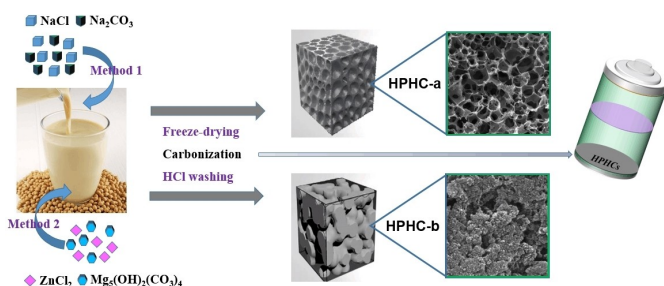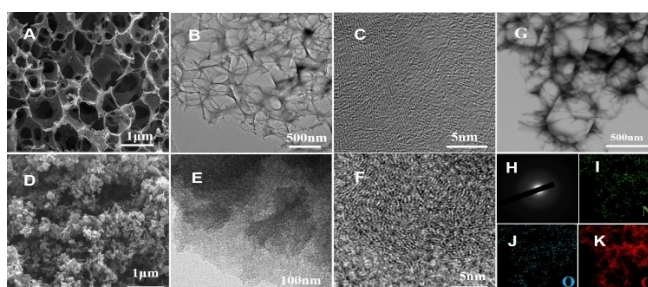

Figure 2. (A, D) FE-SEM images of HPHC-a and HPHC-b respectively; (B, E) TEM images of HPHC-a and HPHC-b respectively; (C, F)HR-TEM images of HPHC-a and HPHC-b respectively; (H) Selected-area electron diffraction pattern of HPHC-a; (G, I, J, K) TEM image and elemental mappings of N, O, C in HPHC-a.
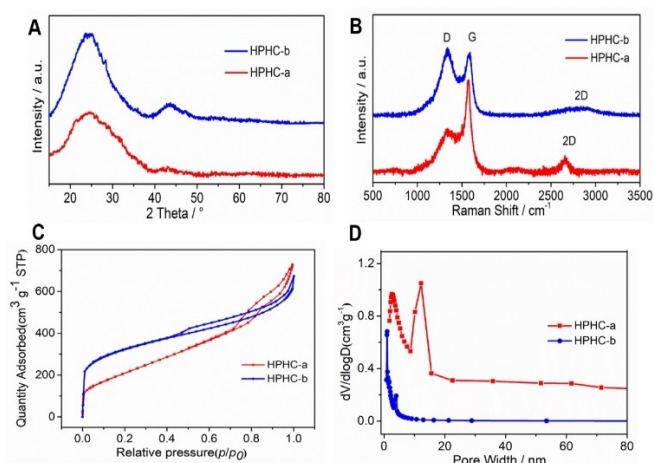

Figure 1. Schematic illustration of the preparation steps for HPHCs.

ChemistryOpen

Full Papers
doi.org/10.1002/open.202000081

**Chemistry
Europe**
European Chemical
Societies Publishing

Figure 3. (A) XRD patterns of the HPHC-a (red) and HPHC-b(blue); (B) Raman spectra of the HPHC-a(red) and HPHC-b(blue); (C, D) N₂ adsorption/ desorption isotherms and pore size distribution of the HPHC-a (red) and HPHC-b(blue), respectively.

the as-carbonized samples exhibit two broad bumps at $\sim 23.4°$ and $\sim 43.5°$, which correspond to the (002) and (100) diffraction modes of graphite structure, respectively. The interlayer distance (002) of graphite structure in each product is calculated to be 0.376-0.384 nm (Table S1) by using the Bragg equation $(2d\sin\theta = n\lambda)$. This value is much larger than that of graphite (0.336 nm), which is in favor of the reversible storage of lithium/ sodium ions. As the carbonization temperature increases, the (100) diffraction peaks became gradually sharpen, suggesting a more ordered crystalline structure (Figure S3). The structural characteristics and graphitization degree of carbonized samples were further elucidated by Raman spectroscopy. The Raman spectra exhibits a broad disorder induced D-band $(\approx 1340 \text{ cm}^{-1})$ and in-plane vibrational G-band $(\approx 1575 \text{ cm}^{-1})$ (Figure 3B). The D-band corresponds to the defects and disorder regions of the material, while the G-band is related to the graphitization degree of the material. The intensity ratio of these two bands (I_G/I_D) is calculated from their integral area, shown in Table S1. The I_G/I_D value of HPHC-a is less than that of HPHC-b, indicating that HPHC-a has more defects due to the heteroatom doping. In addition, a distinct 2D peak was found at 2680 cm^{-1} in HPHC-a, which may due to the formation of a graphene-like structure.[45–46]

It is well known that the specific surface area and pore diameter are also important factors affect the electrode materials properties. In Figure (3C, D), nitrogen adsorption/ desorption isotherms were used to measure the specific surface area and pore distribution of the samples. The sharp absorption of the N₂ adsorption isotherm at p/p0 < 0.1 indicated the presence of abundant micropores. The curve shows a typical I/ IV N₂ adsorption isotherms, indicating that the pore sizes of these samples range from micropores to mesopores.[47] The nitrogen adsorption-desorption isotherms of the samples were further investigated by the BET method to obtain the specific surface area. The corresponding pore-size distribution was calculated according to the HK and BJH models. As is shown in

table S1, the specific surface area of HPHC-a is 764 m²g⁻¹and the HPHC-b is 1097 m²g⁻¹. From the Figure 3D, the pore size of HPHC-a is around 10~15 nm, while the pore size of HPHC-b is mainly around 1~5 nm, indicating the HPHC-a has more mesopores.

To further analysis the chemical composition of the sample, XPS measurement was carried out. The survey XPS spectrum of HPHCs shows three obvious peaks assigned to C1s, O1s and N1s (Figure S4a), which are consistent with the result of elemental mappings in Figure 2. The contents of various elements are shown in the table S2. The comparison of the two carbon materials show that, HPHC-a contains more nitrogen than HPHC-b, possibly because the nitrogen is more easily lost at high temperatures.[53] The N1s spectrum of HPHC-a can be deconvoluted into three components [N-6 (398.4 eV); N-Q (400.4 eV); N-X (402.6 eV)], which are attributed to pyridinic nitrogen, quaternary nitrogen and oxidized nitrogen, respectively. For HPHC-b, it can be fitted by four individual component peaks [N-6 (398.09 eV); N-5(399.69 eV); N-Q (401.2 eV); N-X (402.59 eV)], which are attributed to pyridinic nitrogen, pyrrolic or pyridonic nitrogen, quaternary nitrogen and oxidized nitrogen, respectively.[48,49]

It's widely known that the pyridinic nitrogen (N-6) and pyrrolic (N-5) can create defects to provide active sites for Li/ Na-ion storage, while the graphitic-N(N-Q) could improve the electron transfer.[49–51] Moreover, research shows that pyridinic-like N is more favorable for lithium storage and reversible capacity for the materials than the pyrrolic N.[53] As shown in table S2 the pyridinic N (N-6) in HPHC-a is far more than HPHC-b. The detailed O1s spectra can be deconvoluted into oxygen atoms in C=O at 530.99 eV, C—O—C at532.39 eV and/or C—OH at 533.09 eV in Figure 4(B, D).[53] These types of oxygen-containing surface functional groups are well known to influence the capacity of the engineered carbon due to their high reactivity.[54,55] In addition, a detailed C1s spectrum is dominated by carbon atoms consisting of the C—C bond at 248.8 eV (diamond and graphite types), C—O bond at 286.1 eV, and C=O O—C=O bond at 288.39 eV (Figure S4).
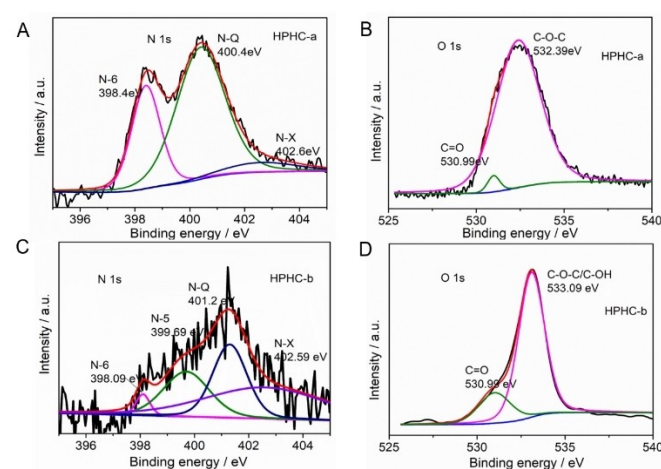

Figure 4. (A, B) N 1s and O 1s core level XPS spectra fitting of the HPHC-a; (C, D) N 1s and O 1s core level XPS spectra fitting of the HPHC-b.

ChemistryOpen

Full Papers
doi.org/10.1002/open.202000081

**Chemistry
Europe**
European Chemical
Societies Publishing

The cyclic voltammograms of HPHCs obtained by different template methods are similar and they all belong to the characteristic of hard carbon anode materials (Figure 5). In the first cycle of the two samples, there are irreversible cathodic peaks around 0.8 V and 1.5 V, and for HPHC-b, there was another irreversible cathodic peak around 1.2 V. These irreversible cathodic peaks correspond to the formation of solid electrolyte interface (SEI) layer during the first discharge process.[56,57] There are a pair of obvious redox peaks in the low voltage range of 0.001–0.3 V, and a pair of weak broad peaks at 1.25 V, corresponding to the plateau region and the slope region of the charge-discharge curve, respectively. This illustrates the storage mechanism of lithium ions in HPHCs. In the subsequent cycles, the CV curves of HPHCs are well overlapped, indicating good cycle stability and reversibility for lithium storage.

Figure 6 (A, B) shows the cycling performance of HPHCs as anodes for LIBs. For HPHC-a, it could deliver a high and stable capacity of about 710 mAh·g^{-1} after 300 cycles at 0.1 A·g^{-1}. For HPHC-b, it could deliver a stable capacity of about 610 mAh·g^{-1} after 200 cycles. The high lithium storage capacity of HPHCs can be attributed to the development of hierarchical porous interconnect structure throughout the pyrolysis process and the heteroatoms doped in the carbon, which can provide abundant active sites for lithium storage. Furthermore, compared with HPHC-b, the HPHC-a has the honeycomb-like structure containing graphene-like nanosheets and higher nitrogen content, which can significantly increase energy storage capacity. Figure 6(C, D) further displays that HPHCs have an excellent rate performance. Particularly, HPHC-a could provide much higher capacities at different current densities (620, 542, 420, 347, 295, 210 and 705 mAh·g^{-1} at 0.1, 0.2, 0.5, 1, 2, 5 and 0.1 A·g^{-1}, respectively), and when the current density returned to 0.1 A·g^{-1}, the capacity stabilized at 710 mAh·g^{-1}. As for HPHC-b, it provides capacities at different current densities (714, 608, 477, 389, 323, 251 and 600 mAh·g^{-1} at 0.1, 0.2, 0.5, 1, 2, 5 and 0.1 A·g^{-1}, respectively). For HPHC-a at different temperatures, and the carbon bulk at 700 °C, their capacities are only maintained at around 400 mAh·g^{-1} and 260 mAh·g^{-1} at 0.1 A·g^{-1} respectively (Figure S5).

The lithium-storage properties of HPHCs were further investigated by electrochemical impedance spectra (EIS) (Figure S6). The Nyquist plots of HPHCs electrode from 0.01 Hz to 100 kHz consist of one semicircle in the high frequency region and a straight line in the low frequency region. The diameter of a semicircle reflects the charge transfer resistance.[58] It can be seen that the HPHC-b electrode displays smaller semicircle diameter than HPHC-a before cycling, suggesting the HPHC-a has more defects. The HPHC-a cycled exhibit a lower charge transfer resistance than fresh cells, which indicates that after cycle the cell has lower charge transfer resistance. The results show that with the increase of charge-discharge cycle, the diffusion rate of lithium ions is higher, and the charge transfer resistance is lower.

In addition, we further investigated HPHCs as anodes for sodium-ion batteries (Figure S7), It showed that HPHC-a had higher reversible capacity and better rate capability than HPHC-b, due to that HPHC-a possesses honeycomb-like structure and higher nitrogen content in the porous structures. After 900 cycles, the reversible capacity of HPHC-a still remains 210 mAh·g^{-1}. All of the above results indicate the HPHC-a has excellent electrochemical performance. Based on these results, it can be proposed that the synergistic effect of hierarchical porous structure and heteroatom doping is extremely beneficial for lithium storage capacity.

Figure 5. Cyclic voltammograms of (A) HPHC-a and(B) HPHC-b at a scan rate of 0.2 mV s^{-1} as anode for LIBs.

3. Conclusions

In summary, two dual-templating strategies for the preparation of hierarchically porous heteroatom-doped carbon materials using soybean milk precursors have been developed. The as-derived hierarchically porous nitrogen/oxygen-doped carbon materials show excellent electrochemical properties for LIBs and SIBs. Electrochemical results reveal this unique structure can provide stable cycling performance (710 mAh·g^{-1} at 0.1 A·g^{-1} after 300 cycles for HPHC-a, and 610 mAh·g^{-1} at 0.1 A·g^{-1} after 200 cycles for HPHC-b) in Li-ion battery and promising Na-ion storage cycling performance (210 mAh·g^{-1} at 0.1 A·g^{-1} after 900 cycles for HPHC-a) as anodes materials. Further comparative research shows that the honeycomb-like composed of graphene-like sheets and heteroatom-doped in these structures
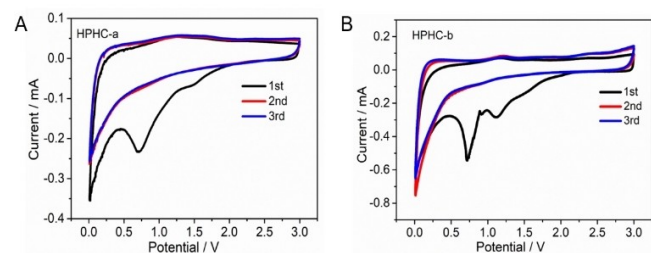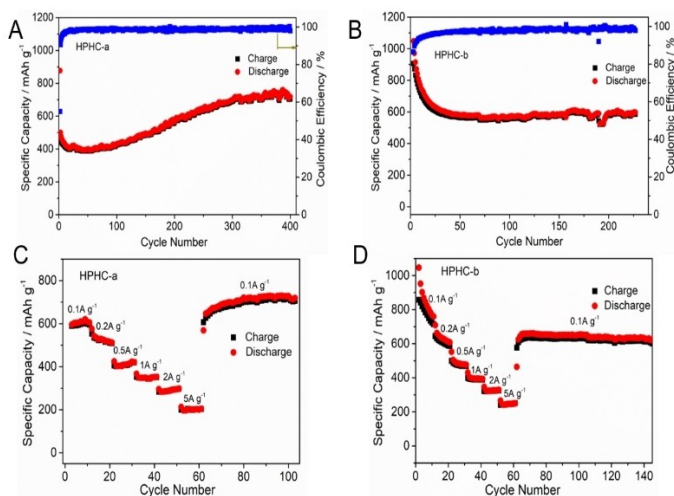

Figure 6. (A, B) Cycling performance and (C, D) rate capacity of the HPHC-a and HPHC-b as LIB anodes, respectively.

ChemistryOpen

Full Papers
doi.org/10.1002/open.202000081

Chemistry Europe
European Chemical
Societies Publishing

are the main reasons for the performance improvement. These graphene-like nanosheets significantly enhanced the intercalation and surface adsorption of Li/Na-ions, and have high charge transfer capacity, and ultimately improved the electrochemical properties of the materials. This work provides novel strategies to design nanostructures by using low-cost carbonaceous materials, thus facilitating their applications as energy storage materials.

Experimental Section

Starting Materials

Soybeans were purchased at local supermarkets. All chemicals are of analytical grade and have not been further purified for use.

Synthesis of 3D HPHCs

The Soybeans are soaked in ultrapure water for 6 hours, and then squeezed into soybean milk with a juicer. Various soluble salts were used as hard templates to construct three-dimensional (3D) porous carbon materials during this experiment. For the preparation of HPHC-a, 8 g of sodium chloride (NaCl, AR, Aladdin) and 0.2 g of anhydrous sodium carbonate (Na_2CO_3, 99.5%, Aladdin) were added to 40 ml soybean milk and was stirred for 1 h. Similarly, for preparing HPHC-b, 3 g of zinc chloride ($ZnCl_2$, 98%, Aladdin) and 1 g of basic magnesium carbonate ($Mg_5(OH)_2(CO_3)_4$, 98%, Aladdin) were added to 40 ml soybean milk and was stirred for 1 h. The resulting solution was rapidly frozen with liquid nitrogen and then freeze-dried at $-55\,°C$ in vacuum. The model of the freeze drying machine is FD-1 A-50(Beijing Biocool Scientific Instruments Co.,Ltd). Finally, the HPHC-a was carbonized at $700\,°C$ for 2 h in a tube furnace under a flowing N_2 atmosphere ($100\ ml\,min^{-1}$). As for HPHC-b, the composite particles were carbonized at $950\,°C$ for 2 h in a tube furnace under a flowing N_2 atmosphere ($100\ ml\,min^{-1}$). During the carbonization process, $ZnCl_2$ is converted to metallic Zn, which can be volatilized at $950\,°C$, at the same time, $Mg_5(OH)_2(CO_3)_4$ is converted into MgO nanocrystallites. Once it's cooled to room temperature, the obtained composite particles were washed with diluted hydrochloric acid (2 M) and the ultrapure water to dissolve the salts and the inorganic impurities that initially exist in the soybean until the filtrate pH=7. Eventually, the pure 3D-HPHCs were obtained. For comparison, the carbon bulks (CB) were also prepared by using the same manner without adding salts.

Characterization

Morphological and structural characteristics of the material were investigated by scanning electron microscopy (SEM, Hitachi S4800) and High (high) resolution transmission electron microscopy (JEOL-2010F) with energy-dispersive spectrometer (EDS). X-ray diffraction patterns (XRD) were obtained on Shimadzu XRD-6000 diffractometer (Cu–Kα radiation, 0.15406 nm). The pore structures and surface areas of the carbon materials were investigated using N_2 physical adsorption/desorption isotherms at 77 K on a BET (ASAP2020) instrument. Prior to adsorption measurement, the samples were outgassed under vacuum for 6 h at $250\,°C$. The X-Ray photoelectron spectroscopy XPS measurements were performed by Thermo ESCALAB250Xi. Raman spectroscopy was tested with a 532 nm laser at room temperature on a confocal microprobe Raman system (RAMAN HORIBA EVOLUTION).

Electrochemical Tests

The electrochemical performance of the 3D HPHCs was analyzed by assembling half-cells in argon-filled glove box. The working electrode was prepared through the following steps: active materials (HPHCs), conductive agent (Super-P) and polymer binder (polyvinylidenefluoridone, PVDF) with a mass ratio of 8:1:1 was mixed with an appropriate amount of NMP (N-methylpyrrolidone) as solvent to prepare slurry. The slury was coated on copper foil that placed in a vacuum oven at $80\,°C$ for 24 h to form an electrode. The active materials on each piece of copper foil is about 0.8 mg. Celgard 2600 and glass fiber were employed as the separators for Li-ion and Na-ion battery, respectively. The counter electrodes were metal-lithium and Sodium disc for Li-ion and Na-ion battery, respectively. The electrolyte was 1 M $LiPF_6$ in the mixed solution (ethylene carbonate/dimethyl carbonate/diethyl carbonate 1:1:1 by volume) for Li-ion battery, and 1 M $NaClO_4$ in the mixed solution (ethylene carbonate / diethyl carbonate 1:1 by volume) for Na-ion battery. The above battery pack were assembled into a CR2032 button half-cell in Argon glove box (O_2 and $H_2O < 1\,ppm$), the ambient temperature is $25\,°C$. The charge/discharge capacity was calculated based on the weight of active materials in the electrodes. The constant current charge and discharge test is on the LAND CT 2001 A battery. The CHI660D workstation (Chen Hua, China) was used to measure cyclic voltammetry ($0.001–3.0$ V, $0.2\ mV\,s^{-1}$) and electrochemical impedance spectra (EIS) (the frequency range 100 kHz–0.01 Hz, and the amplitude of 5 mV).

Conflict of Interest

The authors declare no conflict of interest.

[1] Y. Lin, Z. H. Huang, X. Yu, W. Shen, Y. Zheng, F. Kang, *Electrochim. Acta.* **2014**, *116*, 170.
[2] J. Yang, X. Li, S. Han, R. Huang, Q. Wang, J. Qu, *ChemElectroChem* **2017**, *4*, 2243–2249.
[3] X. Xiao, S. Li, H. Wei, D. Sun, Y. Wu, G. Jin, F. Wang, Y. Zou, *J. Mater. Sci. Mater. Electron.* **2015**, *26*, 1–8.
[4] K. Tian, W. Liu, S. Zhang, R. J. Zeng, H. Jiang, *ChemElectroChem* **2015**, *2*, 859–866.
[5] A. Izadinajafabadi, T. Yamada, D. N. Futaba, M. Yudasaka, H. Takagi, H. Hatori, S. Iijima, K. Hata, *ACS Nano* **2011**, *5*, 811–819.
[6] G. Ye, X. Zhu, S. Chen, D. Li, Y. Yin, Y. Lu, S. Komarneni, D. Yang, *J. Mater. Chem. A* **2017**, *5*, 8247–8254.
[7] J. Cui, Y. Xi, S. Chen, D. Li, X. She, J. Sun, W. Han, D. Yang, S. Guo, *Adv. Funct. Mater.* **2016**, *26*, 8487–8045.
[8] C. Wang, Y. Xiong, H. Wang, C. Jin, Q. Sun, *J. Mater. Chem. A* **2017**, *5*, 15759–15770.

ChemistryOpen

Full Papers
doi.org/10.1002/open.202000081

Chemistry Europe
European Chemical
Societies Publishing

[9] H. Wang, C. Wang, Y. Xiong, C. Jin, Q. Sun, *J. Electrochem. Soc.* **2017**, *164*, A3832-A3839.

[10] Y. Xia, Z. Xiao, X. Dou, H. Huang, X. Lu, R. Yan, Y. Gan, W. Zhu, J. Tu, W. Zhang, *ACS Nano* **2013**, *7*, 7083–7092.

[11] X. Tao, W. Rui, X. Yang, H. Hui, W. Chai, F. Tong, Y. Ga, W. Zhang, *ACS Appl. Mater. Interfaces* **2014**, *6*, 3696–3702.

[12] J. Zhang, J. Xiang, Z. Dong, Y. Liu, Y. Wu, C. Xu, G. Du, *Electrochim. Acta.* **2014**, *116*, 146–151.

[13] J. Guo, J. Zhang, F. Jiang, S. Zhao, Q. Su, G. Du, *Electrochim. Acta.* **2015**, *176*, 853–860.

[14] E. M. Lotfabad, J. Ding, K. Cui, A. Kohandehghan, W. P. Kalisvaart, M. Hazelton, D. Mitlin, *ACS Nano* **2014**, *8*, 7115.

[15] B. Z. Jang, C. Liu, D. Neff, Z. Yu, M. C. Wang, W. Xiong, A. Zhamu, *Nano Lett.* **2011**, *11*, 3785.

[16] C. W. Park, S. H. Yoon, S. I. Lee, S. M. Oh, *Carbon* **2000**, *38*, 995.

[17] Y. C. Xue, T. T. Yu, J. L. Chen, X. H. Wan, X. W. Cai, X. M. Guo, F. Zhang, W. W. Xiong, Y. J. Liu, Q. H. Kong, A. H. Yuan, J. H. Zhang, *J. Solid State Chem.* **2020**, *286*, 121303.

[18] C. Wang, J. Huang, H. Qi, L. Cao, Z. Xu, Y. Cheng, X. Zhao, J. Li, *J. Power Sources* **2017**, *358*, 85.

[19] N. Sun, H. Liu, B. Xu, *J. Mater. Chem. A* **2015**, *3*, 20560.

[20] Y. Zhao, W. Ran, J. He, Y. Song, C. Zhang, D. B. Xiong, F. Gao, J. Wu, Y. Xia, *ACS Appl. Mater. Interfaces* **2015**, *7*, 1132.

[21] F. Cheng, W. Liu, Y. Zhang, H. Wang, S. Liu, E. Hao, S. Zhao, H. Yang, *J. Power Sources* **2017**, *354*, 116.

[22] H. Yu, W. J. Zhu, H. Zhou, J. F. Liu, Z. Yang, X. C. Hu, A. H. Yuan, *RSC Adv.* **2019**, *9*, 9577.

[23] F. F. Zheng, C. Wang, T. T. Meng, Y. Zhang, P. H. Zhang, Q. Shen, Y. C. Zhang, J. F. Zhang, J. X. Li, Q. H. Min, J. N. Chen, J. J. Zhu, *ACS Nano* **2019**, *13*, 12577–12590.

[24] F. Zheng, W. Xiong, S. Sun, P. Zhang, J. J. Zhu, *Nat. Photonics* **2019**, *8*, 391–413.

[25] E. Hao, W. Liu, S. Liu, Y. Zhang, H. Wang, S. Chen, F. Cheng, S. Zhao, H. Yang, *J. Mater. Chem. A* **2017**, *5*, 2204.

[26] J. Wang, P. Nie, B. Ding, S. Dong, X. Hao, H. Dou, X. Zhang, *J. Mater. Chem. A* **2017**, *5*, 2411.

[27] J. B. Song, C. Y. Zhang, J. H. Zhang, H. Zhou, L. Chen, L. L. Bian, A. H. Yuan, *J. Nanopart. Res.* **2019**, *21*, 90.

[28] K. M. Meek, Y. A. Elabd, *J. Mater. Chem. A* **2015**, *3*, 24187.

[29] X. M. Guo, C. Qian, R. H. Shi, W. Zhang, F. Xu, S. L. Qian, J. H. Zhang, H. X. Yang, A. H. Yuan, T. X. Fan, *Small* **2019**, *15*, 1804855.

[30] X. M. Guo, C. Qian, X. H. Wan, W. Zhang, H. W. Zhu, J. H. Zhang, H. X. Yang, S. L. Lin, Q. H. Kong, T. X. Fan, *Nanoscale* **2020**, *12*, 4374–4382.

[31] G. Y. Xu, J. P. Han, D. Bing, N. Ping, P. Jin, D. Hui, H. S. Li, X. G. Zhang, *Green Chem.* **2015**, *17*, 1668–1674.

[32] N. Guo, L. Min, W. Yong, X. Sun, W. Feng, Y. Ru, *ACS Appl. Mater. Interfaces* **2016**, *8*, 33626–33634.

[33] T. Z. Yang, T. Qian, M. F. Wang, X. W. Shen, N. Xu, Z. Z. Sun, C. L. Yan, *Adv. Mater.* **2016**, *28*, 539–545.

[34] X. Zheng, X. Cao, X. Li, J. Tian, C. Jin, R. Yang, *Nanoscale* **2017**, *9*, 1059–1067.

[35] W. Ding, L. Li, K. Xiong, Y. Wang, W. Li, Y. Nie, S. Chen, X. Qi, Z. Wei, *J. Am. Chem. Soc.* **2015**, *137*, 5414–5420.

[36] A. R. Kamali, D. J. Fray, *Carbon* **2013**, *56*, 121–131.

[37] X. Fan, X. Jiang, W. Wang, Z. Liu, *Mater. Lett.* **2016**, *180*, 109–113.

[38] P. Lu, Y. Sun, H. Xiang, X. Liang, Y. Yu, *Adv. Energy Mater.* **2018**, *8*, 1702434.

[39] Y. P. Gao, Z. B. Zhai, K. J. Huang, Y. Y. Zhang, *New J. Chem.* **2017**, *41*, 11456–11470.

[40] Z. S. Wu, Y. Sun, Y. Z. Tan, S. Yang, X. Feng, K. Mullen, *J. Am. Chem. Soc.* **2012**, *134*, 19532–19535.

[41] X. Liu, J. Zhang, S. Guo, N. Pinna, *J. Mater. Chem. A* **2016**, *4*, 1423–1431.

[42] Z. S. Wu, W. C. Ren, L. Xu, F. Li, H. M. Cheng, *ACS Nano* **2011**, *5*, 5463–5471.

[43] X. Wang, Q. Weng, X. Liu, X. Wang, D. M. Tang, W. Tian, C. Zhang, W. Yi, D. Liu, Y. Bando, D. Golberg, *Nano Lett.* **2014**, *14*, 1164–1171.

[44] Y. Sun, R. Y. Zhong, H. Z. Zhang, T. Z. Huang, J. M. Yu, H. Y. Fang, D. Liang, Z. Q. Guo, *Int. J. Hydrogen Energy* **2019**, *44*, 21790.

[45] W. Xing, S. Z. Qiao, R. G. Ding, F. Li, G. Q. Lu, Z. F. Yan, H. M. Cheng, *Carbon* **2006**, *44*, 216.

[46] J. Y. Li, H. Qi, Q. G. Wang, Z. W. Xu, Y. J. Liu, Q. Y. Li, X. G. Kong, J. F. Huang, *Electrochim. Acta.* **2018**, *271*, 92.

[47] J. Zhao, Y. F. Jiang, H. Fan, M. Liu, O. Zhuo, X. Z. Wang, Q. Wu, L. J. Yang, Y. W. Ma, Z. Hu, *Adv. Mater.* **2017**, *29*, 1604569.

[48] B. Zhang, Y. Yu, Z. L. Xu, S. Abouali, M. Akbari, Y. B. He, F. Kang, J. K. Kim, *Adv. Energy Mater.* **2014**, *4*, 1301448.

[49] B. Li, F. Dai, Q. Xiao, L. Yang, J. Shen, C. Zhang, M. Cai, *Energy Environ. Sci.* **2016**, *9*, 102–106.

[50] M. Yang, Z. Zhou, *Adv. Sci.* **2017**, *4*, 1600408.

[51] J. Gu, Z. Du, C. Zhang, S. Yang, *Adv. Energy Mater.* **2016**, *6*, 1600917.

[52] J. Ding, Z. Li, K. Cui, S. Boyer, D. Karpuzov, D. Mitlin, *Nano Energy* **2016**, *23*, 129–137.

[53] J. Ou, Y. Zhang, L. Chen, Q. Zhao, Y. Meng, Y. Guo, D. Xiao, *J. Mater. Chem. A* **2015**, *3*, 6534–6541.

[54] B. Li, F. Dai, Q. Xiao, L. Yang, J. Shen, C. Zhang, M. Cai, *Adv. Energy Mater.* **2016**, *6*, 1600802.

[55] B. Li, F. Dai, Q. Xiao, L. Yang, J. Shen, C. Zhang, M. Cai, *Energy Environ. Sci.* **2016**, *9*, 102–106.

[56] D. D. Li, L. Zhang, H. B. Chen, J. Wang, L. X. Ding, S. Q. Wang, P. J. Ashman, H. H. Wang, *J. Mater. Chem. A* **2016**, *4*, 8630–8635.

[57] S. Q. Wang, L. Xia, L. Yu, L. Zhang, H. H. Wang, X. W. Lou, *Adv. Energy Mater.* **2016**, *6*, 1502217.

[58] M. Huang, K. Mi, J. H. Zhang, H. L. Liu, T. T. Yu, A. H. Yuan, Q. H. Kong, S. L. Xiong, *J. Mater. Chem. A* **2017**, *5*, 266.